Hydroxyapatite nanoparticle mesogens: getting closer and closer to bone mimetic platforms

*Luciano A. Benedini [a §], Yanina Moglie [a §], Juan M. Ruso [b], Sofía Nardi [a] and Paula V. Messina [a]**

(a) INQUISUR – CONICET, Department of Chemistry, Universidad Nacional del Sur, B8000CPB, Bahía Blanca, Argentina. (b) Soft Matter and Molecular Biophysics Group, Department of Applied Physics, University of Santiago de Compostela, 15782 Santiago de Compostela, Spain.

* Author to whom correspondence should be addressed. Tel: +54 291 4595159. Fax: +54 291 4595160. Electronic mail: pmessina@uns.edu.ar.

§ They have the same participation in this work

Abstract

Biological molecular networks exhibit lyotropic liquid crystalline (LLC) properties that can support non-equilibrium pathways influenced by dynamic processes at the microscale. With the aim of take a further step towards the conquest of a biomimetic material to apply in calcified tissues regeneration, in this work, we have evaluated the anchorage of N-C-P and C-N-P molecular fragments on previously investigated biomimetic hydroxyapatite nanoparticles (nano-HA). Following we have assessed the effect of the type and degree of substitution over the spontaneous self-association of acidic macromolecules that respond to

pH stimulation. Produced materials were inspected by Fourier transform infrared (FT-IR) and solid state nuclear magnetic resonance (MAS-RMN) spectroscopy, small angle X-ray scattering (SAXS), powder X-ray diffraction (XRD), differential scanning calorimetry (DSC), thermogravimetric analysis (TGA), polarized light (PLM) and high resolution electron transmission (H-TEM) microscopy. A complete analysis of experimental data proved that under specific synthetic conditions it is possible to obtain substituted-HA nanoparticles that are able to act as mesogenic agents inducing, at concentration values analogous to biogenic ones, a LLC structure on acidic macromolecules organization. These systems that dynamically respond to pH can be adapted *in vitro* to achieve original and improved engineered biomaterials for tissue restoration therapies.

1. Introduction

It has long been recognized that the multifaceted self-organization of dynamic living systems, associated to a wide-range of precise biological functions, exhibits liquid crystalline mesoscopic order.[1-3] An unparalleled example is the hierarchical 3D nano-architecture constituted by lyotropic nematic phases and rod-like nano-apatites within the collagen matrix, where the latter have a clear influence on the organization [4] and properties [5, 6] of the final assembly.

Integration of inorganic lyotropic liquid crystals (iLLCs) into engineering biomaterials has formidable benefits such as biomimicry, spontaneous arrangement, easy bottom-up processing, direct up-scaling, self-replication and minimal energy inputs. [7] However, this aspect has not yet been properly recognized among scientists belonging to the disciplines of tissue engineering and regenerative medicine. [2, 3] As far as our knowledge, the design of biocompatible nano-apatite lyotropic liquid crystals platforms has begun to be very recently

explored. [5, 8, 9] Along this line, we have successfully created bone-mimetic hydroxyapatite nano-rods (nano-HA) [10-12] that coerce, with a straight concentration dependence, the interactions among hydrolyzed collagen peptide units, [13] sodium alginate, [14, 15] membrane phospholipids, [11] soluble blood serum proteins [16, 17] and blood plasma. [18] Furthermore, 3D gelatin fiber mesh and sodium alginate scaffolds reinforced with our nano-HA displayed a mineralization [13-15] and a mechanical [15, 19] performance that validate their use in bone therapies.

In this investigation we take a further step towards the biomimicry concept by awarding mesoscopic order to amino phosphorous nano-HA derivatives and guiding the substrate morphology using acidic macromolecules under pH stimuli similar to that exhibits collagen type I *in vivo*. [20] The obtained iLLCs textures, observed under polarized light displayed a disturbed hexagonal mesophase much like to the columnar phase in discotic liquid crystals, where the conjugated N–C–P and C–N–P molecules are covalently attached to the nano-HA surface. The N–C–P molecular fragment has a broad biological relevance, emerging as the main accepted treatment for patients with osteoporosis or bone lesions caused by advanced solid tumors or multiple myelomas. [21] We believe that crucial features of N–C–P can be transmitted and regulate by the activity of the assemblies that include it, avoiding the problems associated to their systemic circulation. [22]

This work is a contribution towards the development of new types of inorganic LLCs, but, above all, it is a crucial step in the direction of our final goal: the transference of biomimetic order, flexibility, mechanical integrity and the specific functionality of phosphorus derivatives to a dynamic nano-HA / hydrogel matrix.

2. Experimental Section

2.1 Reagents

Triblock poly(ethylene glycol)-poly(propylene glycol)-poly(ethylene glycol) copolymer Pluronic® F-127 ($EO_{102}PO_{70}EO_{102}$, CAS n° 9003-11-6, BioReagent, Sigma - Aldrich); polyethylene glycol (20) sorbitan monostearate (Tween® 60, CAS n° 9005-67-8, Sigma - Aldrich); sodium phosphate tribasic dodecahydrate ($Na_3PO_4 \cdot 12H_2O$, CAS n° 10101-89-0, Sigma - Aldrich); calcium chloride ($CaCl_2$, CAS n°10043-52-4, Sigma - Aldrich); phosphate buffer saline (PBS tablets, Na_2HPO_4 / NaH_2PO_4, MFCD00131855, Sigma - Aldrich); acetic acid ($C_2H_4O_2$, CAS n° 64-19-7, Sigma - Aldrich); sodium acetate trihydrate ($C_2H_3NaO_2 \cdot 3H_2O$, CAS n° 127-09-3, Sigma - Aldrich); ethanol (EtOH, CAS n° 64-17-5, Sigma – Aldrich); methanol (MetOH, CAS n°67-56-1, Sigma – Aldrich); 3-(aminopropyl)triethoxysilane (APTES, CAS n° 919-30-2, Sigma – Aldrich); tetrahydrofuran (THF, CAS n° 109-99-9, Sigma – Aldrich); triethylamine ($(C_2H_5)_3N$, CAS n° 121-44-8, Sigma – Aldrich); dichloromethane (CH_2Cl_2, CAS n°75-09-2, Sigma – Aldrich); acetonitrile (C_2H_3N, CAS n°75-05-8, Sigma – Aldrich); potassium bromide (KBr, CAS n° 7758-02-3, Supelco for IR spectroscopy Uvasol®) and polyacrylic acid (PAA, $[-CH_2-CH(CO_2Na)-]_n$, CAS n° 9003-01-4, MW = 104.4 kDa, 52 - 68% of carboxylic groups, Supelco) was used without further purification. Solvents were purified and dried by standard methods prior to use. Anhydrous THF was freshly distilled from sodium/benzophenone. Dry CH_2Cl_2 was obtained by refluxing solvent on calcium hydride for an hour and distilled under nitrogen. For crystal liquid preparation, only Milli-Q water was used.

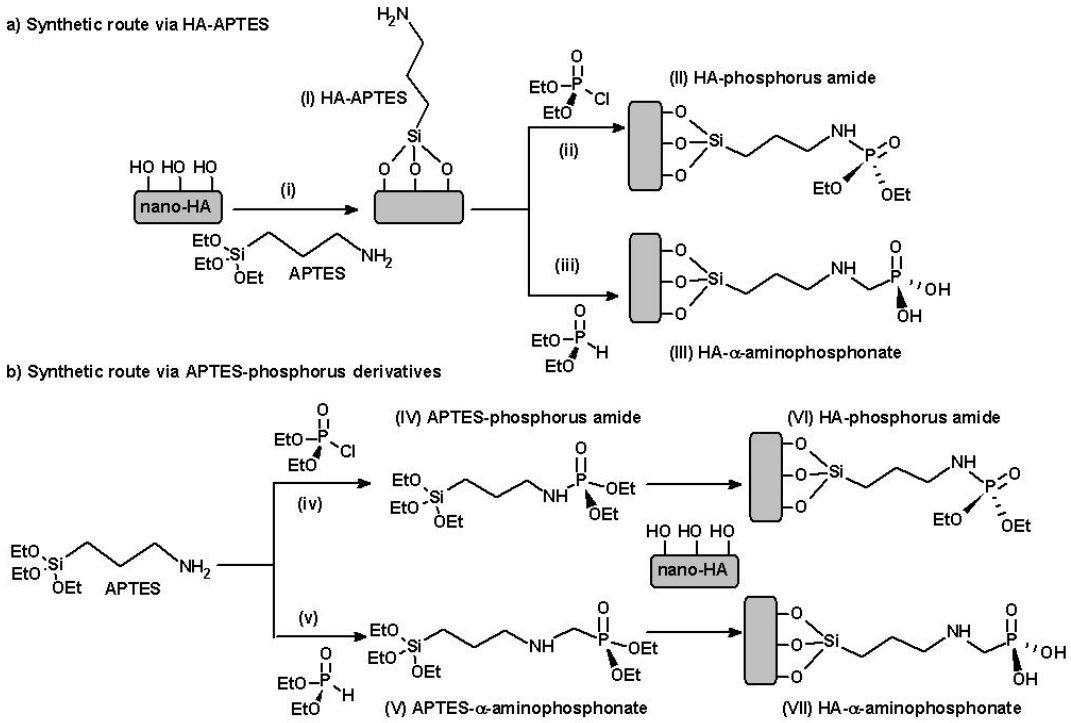

Scheme 1. Grafting strategies for the production of different HA-amino phosphorus derivatives: (a) synthetic route via HA-APTES reaction, (b) synthetic route via APTES-phosphorus derivatives. pH of reaction media >7.0.

2.2 Functionalized nano-hydroxyapatite

2.2.1 Strategies of surface modification

Bone-like HA nanoparticles (nano-HA) with an isoelectric point (IP) of 3.1 – 3.4 [16] were prepared and characterized following a previously described procedure. [12] For the creation of HA-amino phosphorus derivatives, modified synthetic routes mediated by APTES [23, 24] were investigated, **scheme 1**. To evaluate the effect of the N–C–P group on the mesophase

organization, both phosphorus amide (C–N–P) and α-aminophosphonate (N–C–P) groups were grafted on nano-HA surfaces.

2.2.1.1 nano-HA functionalization via HA-APTES reaction

i) First 500 mg of nano-HA and 200 mL ethanol were placed in a 250 mL balloon. The mixture was sonicated during 6 h until a homogeneous solution was obtained. Following, 5 mL APTES and 1 mL Milli-Q water were added to facilitate the hydrolysis of the alkoxysilane groups. This mixture was vigorously stirred for 16 h at room temperature (RT). Then, reaction mixture was washed twice with 100 mL water and centrifuged at 4000 rpm; the procedure was repeated another 2 times with 100 mL methanol. The solid obtained was dried under vacuum for 3 h. Two batches of 417.9 mg and 434.0 mg white solids of functionalized nano-HA with aminopropyltriethoxysilane (HA-APTES) were obtained. ii) For the functionalization of nano-HA with phosphorus amide group, 417.9 mg of HA-APTES were placed in a conical balloon previously dried and purged with N_2. Then, 10 mL THF and 2.680 mL triethylamine were added at 5 °C. To this mixture, a solution of 2.880 mL of diethylchlorophosphate in THF (5 mL) was added drop wise. The reaction was stirred for 2 h at 5 °C and then at 40 ° C for 16 h. The reaction product was washed twice with 100 mL water and centrifuged at 4000 rpm; the procedure was repeated another 2 times with 100 mL methanol. The separated material was dried under vacuum for 3 h and finally 352.3 mg of a pale orange solid was obtained ((II) HA-phosphorus amide, II-HA-PA).

iii) The functionalization of nano-HA with α-aminophosphonate group is carried out via three-component coupling of HA-APTES (amine), dichloro methane and diethyl phosphite. 434.0 mg HA-APTES were placed in a conical balloon previously dried and purged with N_2. Then, 14 mL of an equivolumetric solution of dichloromethane and acetonitrile were added at RT. Following, 851.2 μL of diethyl phosphite (6.65 mmol) was added to this mixture and a pre-dried and N_2 purged refrigerant was adjoined to the balloon. The reaction

mixture was stirred and heated at 75° C for 3 days. The reaction product was washed twice with 100 mL water and centrifuged at 4000 rpm; the procedure was repeated another 2 times with 100 mL methanol. The separated material was dried under vacuum for 3 h and finally 340.7 mg of a white solid ((III) HA-α aminophosphonate, III-HA-αAP) was obtained.

2.2.1.2 nano-HA functionalization via APTES-phosphorus derivatives

This synthesis was carried out modified the method proposed by Dudarko *et al*. [26] In a conical balloon, previously dried and purged under N_2, 4.690 µL APTES (20 mmol), 2.780 mL triethylamine (20 mmol) and 10 mL of tetrahydrofuran (THF) as solvent were placed.

iv) The mixture was stirred at 5 °C for 1 h and then a solution of diethylchlorophosphate (2.880 µL, 20 mmol) in 5 mL THF was added. The mixture was stirred for a further 2 h at 5 °C and next for 2 h at 40 ° C. Then, 20 mL of dichloromethane were added to the reaction crude. The obtained ammonium salt was filtered and the reaction crude was washed twice with 15 mL of Milli-Q water and dried with anhydrous sodium sulfate. The solvent was evaporated and yellow oil of (IV) APTES-phosphorus amide (IV-APTES-PA) was obtained which was used to functionalize the nano-HA. The product was confirmed through ^{1}H and ^{31}P nuclear magnetic resonance spectroscopy (NMR, Bruker Avance III). To functionalize nano-HA, we proceed in the same way as in the previous section (i) but instead of using APTES the compound IV-APTES-PA was used. A white solid (399.9 mg) called (VI) HA-phosphorus amide (VI-HA-PA) was obtained.

v) At RT, 851.2 µL diethyl phosphite (6.650 mmol) was added to this mixture and a pre-dried and purged N_2 refrigerant was added to the balloon. The reaction mixture was stirred and heated at 75° C throughout 3 days. Then, the solvent was evaporated and yellow oil

called (V) APTES-α-aminophosphonate (V-APTES-αAP) was obtained. The reaction mixture was passed through gas chromatography–mass spectrometry (GC-MS, Thermo Scientific MSQ PLUS) and the starting substrate (APTES) could be observed with respect to the expected product in a 3: 1 ratio; this was also confirmed through ^{1}H and ^{31}P NMR (Bruker Avance III).

To functionalize the HA, the procedure was the same as in the previously descript section (i) but instead of using APTES the compound V-APTES-αAP was used. A white solid (300.0 mg) called (VII) HA-α-aminophosphonate (VII-HA-αAP) was obtained.

In all experiments, the reaction pH was monitored with an ION 510 Benchtop Meter (OAKTON Instruments) and confirmed that remained > 7 throughout the procedure. *2.2.2 Characterization techniques*

Fourier transform infrared (FT-IR) spectra were recorded using a Nicolet Nexus 470 spectrophotometer (Thermo Electron Corporation, Waltham, MA). All spectra were recorded in transmission mode, ranging from 400 to 4000 cm^{-1}, at RT with a resolution of 2 cm^{-1} and a rate of 64 scans min^{-1} using an AVATAR Smart Diffuse Reflectance Accessory. After measurements, samples were dispersed in dry KBr (1%Wt.); for the background, a micro-sample cup of pure dry KBr was prepared.

X-ray powder diffraction (XRD) data were acquired with a Philips PW 1710 diffractometer associated to a Cu Kα radiation source(λ = 1.5418 nm) and a graphite monochromator operated at 45 kV, 30 mA, and RT.

Solid-state nuclear magnetic resonance (NMR) spectroscopy was performed on a Bruker AV 400 WB spectrometer equipped with a 4 mm multi-nuclear (^{1}H, ^{13}C, ^{29}Si and ^{31}P) triple-channel (BL4 X/Y/1H) cross polarized magic angle spinning (CP-MAS) probe. CP-

MAS experiments were performed using a 10 kHz spinning rate and a 3.5 ms contact time. Superimposed peaks were de-convoluted using Gaussian fits; each record was done almost in triplicate.

2.3 Inorganic lyotropic liquid crystals (iLLC)

Polyacrylic acid hydrogels (PAA-HG) were prepared by adding 25 µL of nanoparticles (HA, VI-HA-PA, VII-HA-αAP, III-HA-αAP) previously suspended in PBS (10 mg / mL) to 25µL of PPA dissolved in PBS (3 mg / mL). Following, the incorporation of nanoparticles in the hydrogel structure was observed by high-resolution transmission electron microscopy (H-TEM). H-TEM microphotographs were acquired using a Libra 200 FE OMEGA microscope working at 200 kV of operating voltage that corresponds to a maximum magnification of 1 000 000 ×. Powdered samples were situated on carbon supports of 2000 mesh as required and observations were made in a bright field.

2.3.1 Thermal behavior and dynamic mass loss

The thermal characterizations of iLLCs were determined using a Q20 Differential Scanning Calorimeter (TA Instruments). The temperature and enthalpy scales were calibrated using standard samples of indium (CAS No.7440-74-6/1, T_m = 156.6 °C, ΔH_m = 3.295 kJ mol^{-1}) and zinc (CAS No.7440-66-6/3, T_m = 419.53 °C, ΔH_m = 7.103 kJ mol^{-1}). The iLLC samples had been weighted in a ± 0.00001 g precision balance and sealed in an aluminum pan. Then, they had been cooled to−20 °C during 1 min and heated up to 400 °C at a rate 0.08 ° C seg^{-1}. Ultrapure nitrogen was used as purge gas at a rate of 20 mL^{-1}min during the measurement. The baseline subtraction was made to correct any heat capacity difference between the sample and the reference furnace. All the experiments were done in triplicate.

The specific heat C_p in J g^{-1} K^{-1} of every sample was calculated from the DSC thermogram consisted of heat flow (W g^{-1}) by using equation (1): [27]

$$C_p = Q' \times 60/r \quad (1)$$

where *r* is the heating rate of the process in K min^{-1}, *Q'* is heat flow in W g^{-1}. The resulting data were used to construct specific heat versus temperature curves.

To evaluate the effect of pH, 25 µL of acetate buffer instead of PBS was added to each sample after measurements. Superimposed peaks were de-convoluted using Gaussian fits.

Thermal stability of the samples was investigated via thermogravimetric analysis (TGA) performed in a DSC-TGA, SDT Q600 model, TA Instruments, New Castel, USA. The mass loss was measured from 20 to 120 °C at a rate of 0.08 °C s^{-1} under an air atmosphere.

2.3.2 Morphological characterization

Observation of iLLC organizations along concentration and pH profiles were done by polarized light microcopy (PLM) using a LEICA DM7508 microscope provided with a LEICA DMC2900 camera from Leica Microsystems GmbH, Germany. The samples (1.5 / 5 / 1 of PAA / HA, functionalized HA nanoparticles / water weight ratio) were mounted in a custom-built two-sided open glass micro-chamber, modified accordingly to the methodology proposed by De Sa Peixoto *et al.* [28] Glass micro-chambers were set horizontally for the observation of the fluid state. Slow and continuous evaporation under N_2 gas atmosphere injection (flow-rate = 0.2 µL min^{-1}) gradually increased the PAA content in the glass micro-chamber displaying a gradient from the edge (highest concentration) to the center where the initial solution was placed. To attain the H_2O % Wt. in bone tissue, [29] the loss of 90 % of the total volume was required; in such conditions the

estimated final effective concentration of PAA / HA; functionalized HA nanoparticles / water was of 7.5 / 25 / 1 weight ratio. To study the effects of pH, the samples were left completely evaporate to attain the aforementioned concentration and following acetate buffer (pH = 4.1) was injected through the chamber at 0.2 μL min^{-1}. According to the design of the micro-chambers, [28] acetate molecules freely and uniformly diffused through it; microphotographs were taken every 0.5 minutes as the diffusion front progresses. The pH of the micro-chambers was checked using pH indicators paper (Whatman, pH 0 - 14). All experiments were repeated three times. Structure and structural transitions of HA (or substituted-HA) / PAA - HA hydrogels were evaluated by Small-Angle X-ray Scattering (SAXS) experiments using an Empyrean III (Malvern Panalytical) X-ray Diffractometer based on a multi-functional, floor-standing X-ray scattering platform. The goniometer enables a smallest step size of 0.0001° in 2θ and has a radius of 240 mm. A metal-ceramic, sealed Cu X-ray tube with a long fine focus (dimensions 12 × 0.4 mm^2) is mounted on the omega arm of the goniometer. It is powered by a 4 kW high voltage X-ray generator. The X-ray tube is operated at a voltage of 45 kV and with a current of 40 mA. For SAXS, an elliptically bent, 1D graded, multilayer X-ray mirror focuses the divergent X-ray beam from the source in the equatorial direction on the detector plane. A monochromatic (Cu Kα radiation, with a residual Cu Kβ contamination that amounts 0.1% of the CuKα radiation), highly intense, narrow, line-shaped beam resulted. The beam dimensions on the detector are approximately 130 μmin the equatorial direction and 17 mmin the axial direction. A compact, detachable SAXS/WAXS chamber (ScatterX78, Malvern Panalytical) is mounted. This chamber is evacuated to a vacuum level of below 0.1 mbar to avoid parasitic air scattering. The sample (1.5 / 5 / 1 of PAA / HA, functionalized HA nanoparticles / water

weight ratio) is placed into this chamber in a pre-aligned sample holder. The 2D-detector, PIXel3D (Malvern Panalytical) is mounted behind the exit window of the vacuum path and used in the scanning linear mode (1D). The 2θ range used in these experiments was from -0.1° to 5° with a step size of 0.0016°. The distances from the X-ray source to the sample, as well as from the sample to the detector plane, were of 240 mm, both. Data were presented as the scattered intensity *I (q)* of an elastic scattering event recorded as a function of the modulus of the momentum transfer vector, the scattering vector: $q = 4\pi \sin\theta/\lambda$, where λ is the wavelength and θ is the scattering angle. Radius of gyration, R_g, was estimated by the slope of the linear plot of *I(q)* vs. q^2 accordingly to the Guinier approximation, which states that for very small values of q, the scattered intensity can be described as: [30]

$$I(q) = I(0)e^{\left(-\frac{R_g^2 q^2}{3}\right)} \quad (2)$$

Information about the fractal dimension of the scattering objects was determined by examination of the Porod region fitting experimental data to the following equation: [30]

$$I(q) = {}^{A}/_{q^n}, \quad (3)$$

Accordingly to equation (3), a log (*I (q)*) vs. log (*q)* plot, the Porod's plot, can be used to obtain a power law coefficient related to the local structure, the fractal dimension. At $2\pi/R < q > 2\pi/r_0$, $n = D_m$, where R is the upper limit for the mass fractal structure and r_0 is the primary unit of the aggregate. For surface fractals, $n = 6 - D_s$, here $q >> 2\pi/r_0$. [31]

Degree of flexibility within the scattering particles was analyzed by the visual features in a Kratky plot ($q^2 I(q)$ vs. q). [30]

2.4 Statistical analysis

All quantitative tests were carried out in triplicate, and all values were reported as the mean ± standard deviation (SD). Statistical analysis was carried out by the one-way analysis of variance (one-way ANOVA). [32] The statistical difference between two sets of data was considered significant when $p < 0.05$.

3. Results and Discussion

3.1 Covalent immobilization of bone active molecular groups

3.1.1 Biogenic hydroxyapatite substrate

The use of covalent anchors to modify the surface of bioceramic materials is a promising way to improve its functionality. [33] In this process, the density and surface distribution of attached functional groups, and in turn the final characteristics, are strongly influenced by the chemical nature of the surface where they are anchored. Therefore we begin to characterize the substrate: the hydroxyapatite nanoparticles. Microstructure and physical parameters of bare rod-like HA nanoparticles were widely characterized in previous works, [10-12, 17, 34] here we will focus on the functionalization of its surface, therefore, only the experiments inherent to this process will be shown. In this sense, the chemical composition of HA crystals is a key point because the presence of different groups could affect covalent binding. **Figure 1** displays the FT-IR spectra of unfunctionalized nano-HA. The material shows predominantly phosphate and free hydroxyl absorption bands at 1093 ($\nu_3PO_4^{-3}$), 1036 ($\nu_1PO_4^{-3}$), 612 ($\nu_4PO_4^{-3}$), 559 ($\nu_2PO_4^{-3}$), 3566 (OH stretching) and 632 (OH bending) cm^{-1}. Slight and broad bands observed at the region of 3875 - 3600 cm^{-1} indicate intra-molecular hydrogen bonded water, **figure 1 (i)**, while the weak bands appearing at wave number values of 1600 and 1400 cm^{-1} are indicative of CO_3^{-2} substitution, **figure 1 (ii)**.

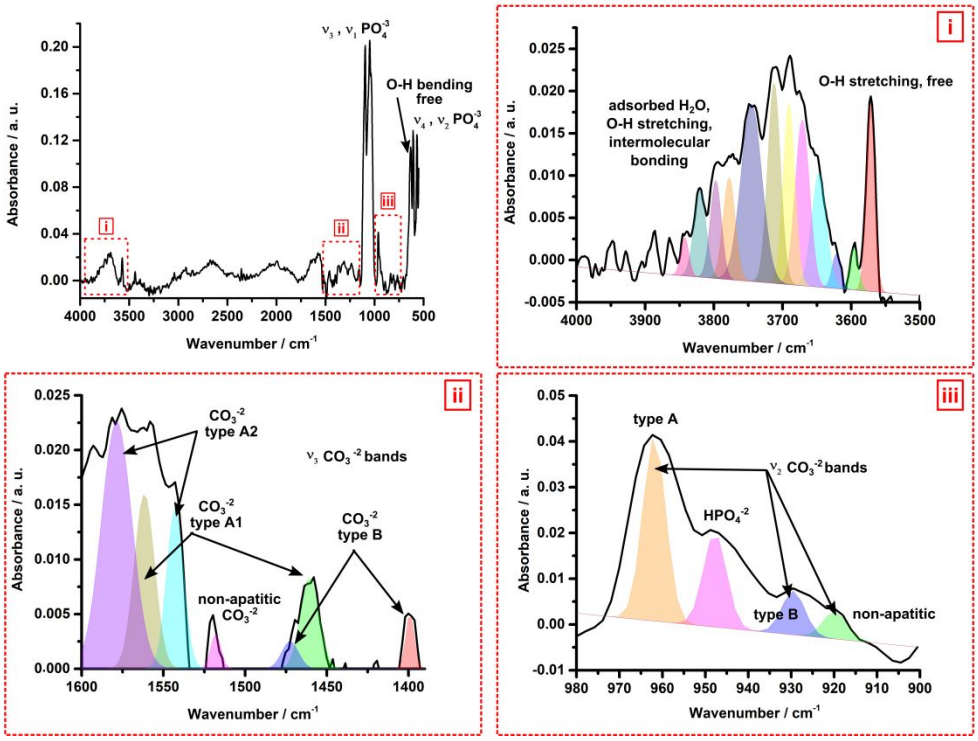

Figure 1. FT-IR of unfunctionalized nano-HA crystals; deconvolution of –OH stretching **(i)**, υ_3 CO_3^{-2} **(ii)** and υ_2 CO_3^{-2} **(iii)** bands.

Deconvolution of the spectra indicates that calcium phosphate nanoparticles are poor crystalized and non-stoichiometric hydroxyapatites exhibiting a certain degree of substitution of the PO_4^{-3} and OH^- ions for HPO_4^{-2} and CO_3^{-2} respectively, **figures 1 (ii)** and **1 (iii)**. In the case of CO_3^{-2}, a mixture of AB substitution type occurs (A type: $CO_3^{-2} \rightarrow OH^-$; B type: $CO_3^{-2} \rightarrow PO_4^{-3}$) with a major proportion of the type A one. From the analysis of 3875 - 3600 cm^{-1} region, **figure 1 (i)**, almost ten peaks can be recognized related to the O - H stretch, they may be assigned to different structural OH^- ions with more or less hydrogen bond association to phosphate groups or forming intra-molecular bonds between hydration water clusters.

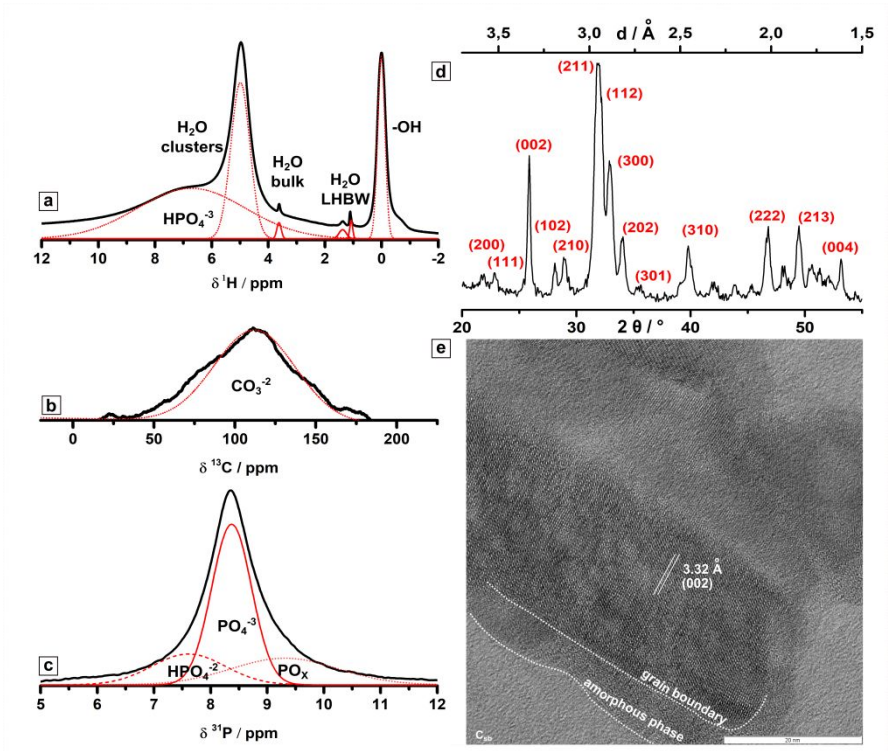

Figure 2. Deconvoluted MAS-NMR spectra of bare nano-HA: **(a)** ^{1}H-NMR, **(b)** ^{13}C-NMR, **(c)** ^{31}P-NMR. **(d)** X-ray diffraction pattern of nano-HA (JCPDS 00-09-0432) and **(e)** H-TEM microphotographs of rod-like HA nanoparticles. C_{sb}: carbon support background.

Replacement of PO_4^{-3} by HPO_4^{-2}, as well as the CO_3^{-2} substitution in the HA crystal lattice was supported by the ^{13}C-NMR and ^{31}P-NMR, **figures 2b** and **2c**. The Wt.% of CO_3^{-2} was about 0.3, computed based on the methodology of Grunenwald *et al.*, [35] while the HPO_4^{-2}/ PO_4^{-3} and HPO_4^{-2}/ OH^- ratios, computed based on FT-IR and ^{1}H-RMN, were 0.05 and 0.34 respectively. Associated ^{1}H- and ^{31}P- NMR full width at half maximum (fwhm) peak from

the $O^{1}H^-$ and $^{31}PO_4^{-3}$ are about $fmhw_{(OH)}$ = 0.33 ppm and $fmhw_{(PO4)}$ = 0.83 ppm and can be related to the organization of the respective groups environment. [36] From literature information, it can be stated that well-ordered HA crystal displays $fmhw_{(OH)}$ = 0.50 ppm and $fmhw_{(PO4)}$ = 0.67 ppm values, [36] confirming a higher structural order of $–OH^-$ group surroundings and a lower organization in the PO_4^{-3} neighborhoods in agreement with a reduced $CO_3^{-2} \rightarrow OH^-$ substitution and a greater $HPO_4^{-2} \rightarrow PO_4^{-3}$ replacement. The ^{1}H -

NMR spectra also displays two strong peaks at about 0 and 5 ppm. The narrow peak at 0 ppm is the signature for the presence of free OH^- groups in the HA crystal while the broad peak at about 5 ppm corresponds to the formation of surface water clusters (SWC). [37] Furthermore, several weak and narrow bands between 1 and 4 ppm were observed and were assigned to low hydrogen bonded water (LHBW) molecules; [37] their amount is negligible compared with SWC. Finally ^{1}H-NMR spectrum displays a signal centered around 7.4 ppm assigned to the ^{1}H chemical shifts of protons in HPO_4^{-2} groups. The exact localization of the structural water molecules and the HPO_4^{-2} ions within biomimetic HA is still unclear. [38] According to the obtained data we assume that HPO_4^{-2} ions are present in the hydroxyapatite's crystal lattice partially replacing PO_4^{-3} and the water molecules are preferred located as (SWC) on a fraction of amorphous non-apatitic layer. Surface structures of the nano-rods were also examined using H-TEM, **figure 2 (e)**. Results show that the nano-HA surface was covered with an amorphous layer of about 4.5 ± 0.5 nm thickness. On the basis of these considerations we are able to affirm that we are in the presence of a bone biomimetic poorly crystalline non-stoichiometric HA, $(Ca^{2+})_{9.5}(HPO_4^{-2})_{0.5}(PO_4^{-3})_{5.5}(CO_3^{-2}(\leq 0.3$ wt.%), $OH^-)_{1.5}$, with a large number of free OH^- surface groups and different degree of structuring SWC; this is in agreement to previous work [10, 12] and literature information. [9, 38, 39]

3.1.1 Anchorage of N-C-P and C-N-P molecular fragments

Different experimental conditions based on the surface silanization mediated by APTES, APTES-phosphorus amide and APTES-α-aminophosphonate were used and compared, MAS-NMR chemical shift of the final obtained products are summarized in **table SI1** of

Supporting Information (SI). The first step of all tested reaction routes involves the coupling of hydrolyzed nano-HA surface -OH groups located on the "*c*" plane of HA crystals [40] with silanol on APTES or APTES derivatives (IV-APTES-PA and V-APTES-αAP). **Figure 3 (a)**, shows the characteristics ^{13}C-RMN chemical shift of APTES molecule on all obtained reaction products, while the δ ^{29}Si-RMN signals are the characteristics of organosiloxanes condensation network, [41] **figure 3 (b)**.

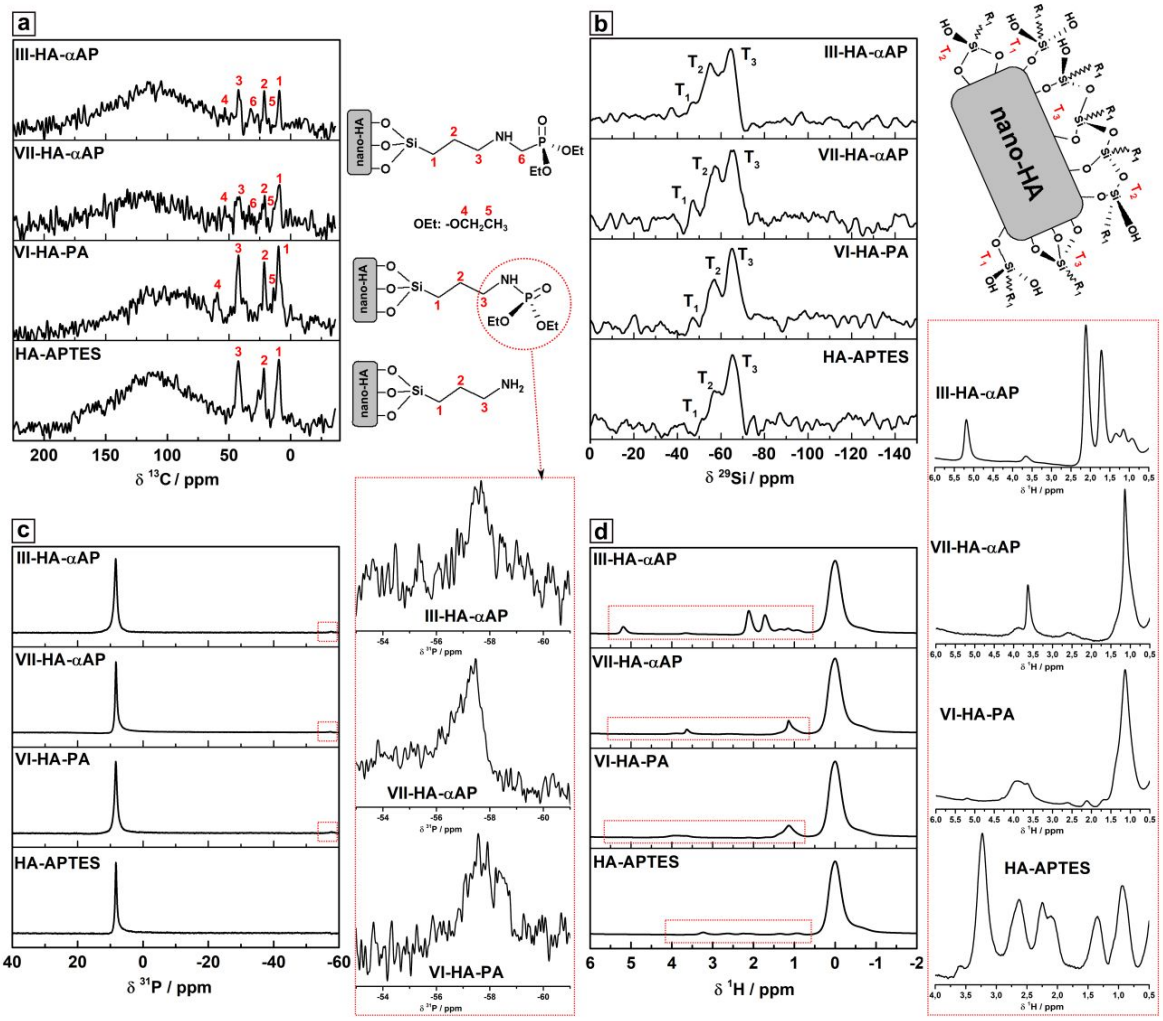

Figure 3. MAS-NMR spectra of functionalized nano-HA. (a)^{13}C-NMR, (b) ^{29}Si-NMR, (c) ^{31}P-NMR and (d) ^{1}H-RMN. R1: -$(CH_2)_3NHCH_2PO(EtO)_2$ or -$(CH_2)_3NHPO(EtO)_2$

Therefore, the obtained product follows a Si–O bond formation between the nano-HA superficial groups followed by the polycondensation of hydrolysed attached APTES derivatives. Regardless of the synthetic route used, no differences were observed in polycondensed silicon structures, **figure 3 (b)**, and all of them showed the presence of superficial polyphosphonate groups (-PO(-OCH_2CH_3)$_2$, δ ^{31}P ≈ -57 ppm), **figure 3 (c)**. From the analysis of ^{1}H-RMN spectra it can be noted that the signal consistent with the SWC (δ ^{1}H ≈ 5 ppm, **figure 2 (a)**) detected in bare nano-HAs has completely disappeared in the functionalized products, **figure 3 (d)**, while the peak assigned to structural free -OH groups (δ ^{1}H ≈ 0 ppm, **figure 2 (a)**) is maintained. At light of the obtained results, we can infer that surface silicon polycondensation on HA nanoparticles majority involves the surface water clusters of the HA and not the lattice -OH groups.

Although the interaction with APTES and APTES derivatives were effective, the degree of functionalization of nano-HA with the R1 chain significantly varies together with the synthetic routes. From the results of ^{1}H-NMR it is seen that only the compound III-HA-αAP shows recognized characteristics of the -$(CH_2)_3NHCH_2PO(EtO)_2$ chain, while for the adducts VII-HA-αAP the peaks are considerably smaller and overlap with the multiple signals of protons in the HA crystal. ^{13}C-NMR signals height, **figure 3a**, confirms that substitution was effectiveness for the III-HA-αAP and VI-HA-PA adducts. The product II-HA-PA was completely missing; the loss of the characteristic signals of the HA-APTES adduct in the 13C-29Si-NMR spectra, please refer to **figure SI1**, indicates that the synthetic route destroys the structure of the intermediary and makes the subsequent reaction impossible to give the final product.

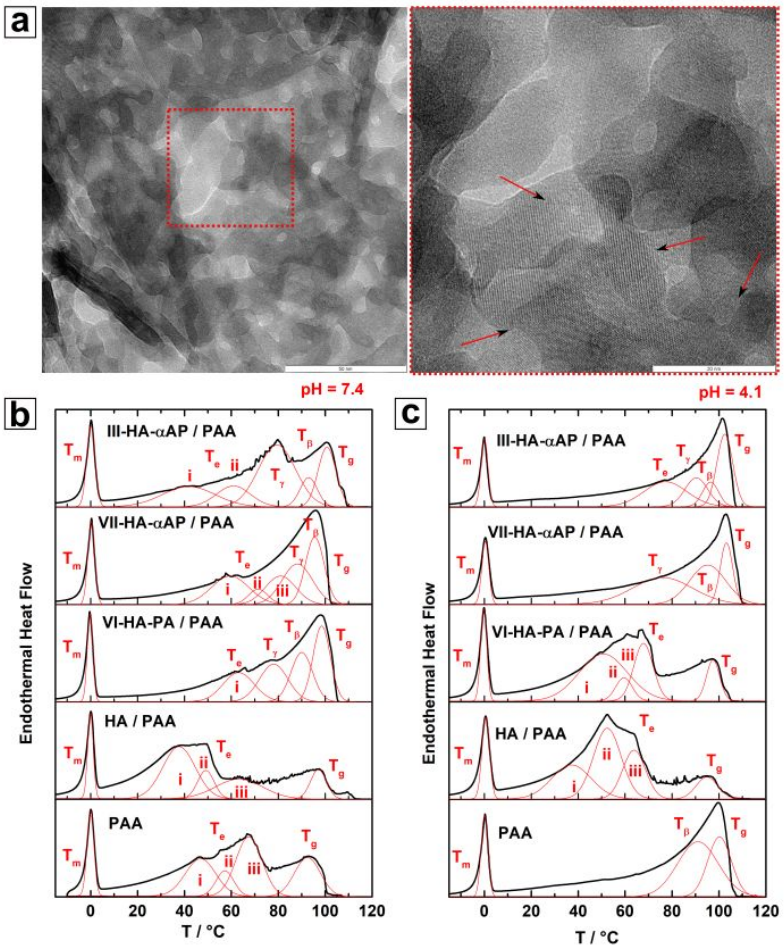

Figure 4. (a) High-resolution transmission electron (H-TEM) microphotographs of HA/PAA-HG, nanoparticles are indicated with an arrow. DSC thermograms of polymer and polymer/nanoparticles hydrogels at **(b)** pH = 7.4 and **(c)** pH = 4.1. Gaussian-peak deconvolution and phase transitions temperatures are shown in red. T_m: water melting point; T_e: water evaporation transitions; T_γ, T_β, T_g: polymer glass transitions.

3.2 Mesoscopic order under pH-stimuli

It is a fact that acidic proteins briefly stabilize the amorphous phase of biogenic hydroxyapatite as precursors of the construction of complex self-organized assemblies [3, 42] and, that the produced crystalline liquid configurations are lyotropic, like most of those that exist in nature, so their organization is influenced by concentration. [3] In an attempt to

examine the influence of HA and functionalized-HA nanoparticles cohesions along a bio-

inspired self-organization approach, the assessment of dynamic control of the iLLC order by the modulation of pH and concentration variables were performed. Polyacrylic acid (PAA) was selected on basis of its high acidic, full of carboxylic groups, dynamic and intrinsically disordered structure; all of them recognized characteristics on nucleation and crystal growth regulation proteins. [43, 44]

3.2.1 Thermodynamic behavior of functionalized nanoparticles assemblies

Insertion of nanoparticles into the polymer framework was confirmed by high-resolution transmission electron microscopy (H-TEM), **figure 4a**; the dynamics of phase-ordering and mass transfer developed as a function of pH were performed by differential scanning calorimetry (DSC) and thermogravimetric analysis (TGA). **Figures 4b and 4c** show the DSC thermograms of PAA, PAA / HA and PAA / functionalized-HA hydrogels (HG) evaluated at pH = 7.4 and 4.1. All thermograms exhibit three characteristics regions ascribed to the following transitions:[45-47] (A) water, melting transition, $T_{m;}$ (B) water, evaporation transition, $T_{e;}$ and (C) polymer, glass transition (T_g). After deconvolution, the identified regions turned out to be the sum of several peaks representing different phase switches; thermodynamic parameters were summarized in **table SI2**. Separate stages of the polymer vitrification transition (T_γ, T_β, T_g) were clearly identified, as well as the influence of HA and functionalized-HA nanoparticles. No changes were observed at $T > T_g$ indicating the thermal stability of samples until 400 °C and that no insoluble PAA anhydride was formed throughout the experiments, **figures SI2- SI11**. [45] At physiological fluid pH conditions, ≈ 7.4, the water in PAA-HG frozen at about 273 K, it behaves like non-bound water (NBW) with nearly bulk water properties, [48] however the obtained

melting transition enthalpy, ΔH_m = 250.6 ± 1.2 J g $^{-1}$, is smaller than ΔH_m of pure water (334 J g^{-1} [49]) in agreement to the molecular clusterization. Consistently, this effect drive a wide-ranging of water dehydration zone among 47 – 67° C [47] and reduced the value of T_g. [48] At pH ≈ 4.1, the NBW evaporation transition (T_e) has practically disappeared and the glassification zone moves towards higher temperatures. A transition at where material acquire toughness was detected (T_β = 91.1 °C, $\Delta H_{\beta\ (pH = 4.1)}$ = 893.6 ± 7.1 J g $^{-1}$) followed by a glass transition exhibiting an increased enthalpy (T_g = 100.3 °C, $\Delta H_{g\ (pH = 4.1)}$ = 561.2 ± 4.2 J g $^{-1}$) respect to the $\Delta H_{g\ (pH = 7.4)}$ = 407.2 ± 2.6 J g $^{-1}$.

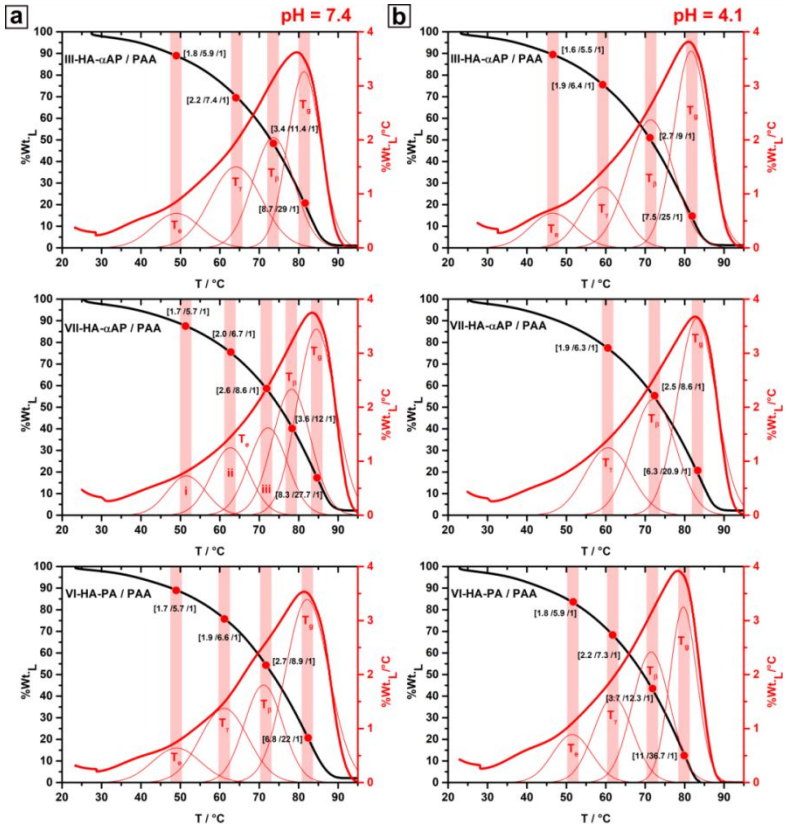

Figure 5. Mass loss (%Wt.$_L$) and thermogravimetric derivative (%Wt.$_L$/°C) profiles of PAA / substituted-HA nanoparticles hydrogels evaluated at pH = 7.4 **(a)** and pH = 4.1 **(b)**. Values of PAA/HA/ W weight ratio at selected points are indicated in square brackets.

Literature information indicates that PAA of molar weight > 16.5 kDa suffers a reversible conformational transition (coil-to-globule transition) around pH = 5 that is driven by the state of ionization of the carboxylic group. [50] At pH = 4.1, PAA assumes a compact and partially globular conformation, while at pH = 7.4 due to carboxylic group ionization the polymer enlarges into a fully solvated open coil configuration. [50] The interaction among nano-HA and PAA molecules at pH = 7.4, probably between $-COO^-$ groups and the positively charged "*a*" plane of HA crystal rich in calcium ions, [40, 44] causes a shift towards low temperatures of the NBW evaporation transition and a reduction in ΔH_g. Surprising, this behavior is maintained at pH = 4.1, whereby the presence of the nanoparticles would be preventing the coil ⇆ globule polymer transition. Interaction of PAA with phosphoroamidates substituted nano-HA inverted the polymer coil ⇆ globule transition, **figures 4b** and **4c**. At pH = 7.4, VI-HA-PA / PAA thermogram shows a shift towards superior temperatures of NBW evaporation and of the PAA glass transitions (T_γ = 76.08, T_β= 90.03 and T_g = 98.53); attributes associated to a compact organization of PAA chains. Nevertheless, at pH = 4.1, the transitions befall on the performance of the polymer coil array. Both at pH = 7.4 and 4.1, VII-HA-αAP / PAA and III-HA-αAP / PAA thermograms display T_e, T_γ, T_β and T_g values characteristics of a high ordered and partially compact polymer association. Thus, interaction of PAA with α-aminophosphonate HA nanoparticles dehydrated and stabilizes the polymer domain organization independently of pH. Mass loss profile and the associated derivative curves of PAA / functionalized-HA hydrogels (HG) are shown in **figure 5**. As can be seen in this figure, there are different regions that match with polymer transitions identified in DSC curves. The transitions in the structure of the polymer respond to changes in the concentration due to water evaporation. Changes took

place at organic component (OC) / hydroxyapatite (HA) / water (W) weight ratios similar to those that occur in bone tissue, [OC / HA /W] = [3 / 6 / 1], [29] no loss of mass was observed above 100 °C.

3.2.2 Modulated oriented structure

Previously confirmed the influence of nano-HA and their substituted forms on the polymer chains arrangement, **figures 4** and **5**, the organization of hydrogels were deeper analyzed with small angle X-ray scattering (SAXS). **Figure 6 a** shows the effect of substituted-HA on the small-angle scattering profiles where *log* (*I(q))* are plotted as a function of *log (q)*; size and form parameters were estimated from the obtained curves, **figures 6b** and **6c**. Two linear zones were defined demonstrating that there is a change of the scattering network along length scales from nm to Å: zone (i), 0.004- 0.011 $Å^{-1}$, where the slope calculated from equation (3) varies from -1.64 for VI-HA-PA / PAA-HG to -1.36 and -1.03 for III- and VII-HA-αAP / PAA-HGs respectively and, zone (ii), 0.011 - 0.230 $Å^{-1}$, where it is about ≈ -3, independently of the nano-HA substitution. The slope value, *n,* in the case of polymer coils, is related to the excluded volume parameter and a value of $n = 5/3$, as the obtained for VI-HA-PA / PAA-HG, is found for fully swollen coils. Nevertheless, a Porod power law of $n = 1$, as the obtained for VII-HA-αAP / PAA-HG, agreed to a scattering from rigid rods. The obtained value for III-HA-αAP / PAA-HG corresponds to an intermediate situation among swollen coils and rigid rods. These results agreed to our previous results, figures **4b** and **4c**, indicating that the substitution of HA by VII-HA-αAP and III-HA-αAP leads to a superior polymer organization at pH = 4.1, while the substitution by VI-HA-PA generates an inversion of the coil-to-globule transition. To

globally quantify the hydrogel network morphology at two distinct length scales, we fitted experimental data to the models proposed by Panyukov-Rabin [51] and Hule *et al*. [52]; equations (4) and (5) respectively. The model of Panyukov-Rabin described the behavior of randomly cross-linked polymer gels, starting from a microscopic model of a network made of instantaneously cross-linked Gaussian chains with excluded volume:

$$I(q) = \frac{A}{1+\xi^2 q^2} + \frac{B}{(1+E^2 q^2)^2} \quad (4)$$

where ξ and E are the "blob" and nano-complex size in the hydrogel network. Our systems proved to be more complex than regular polymer organizations, so the model, as we expected, does not fit the experimental data. The model of Hule et al., settled to evaluate the intra-molecular folding and the consequent intermolecular self-assembly into a cytocompatible hydrogel, best described our samples, but it is not suitable enough.

$$I(q) = \frac{A}{q^n} + \frac{C}{[1+(Lq)^m]} \quad (5)$$

Here, the network scattering at low-*q* regime is described by a Porod-like scattering term, A/q^n, and the high-*q* scattering is expressed by a Lorentzian function that has been used to characterize polymer/solvent interactions and chain solvation features, $C/[1 + (Lq)^m]$. Porod's law describes the asymptotic behavior of the intensity as a function of scattering vector and it is one of the basic formulae in SAXS. [53] However, our obtained results showed that all our systems present a positive deviation to Porod's law, [53] **figure SI12**, resulting in a not entirely good convergence of equation (5), **figure SI13**. This kind of deviation is characteristic of a quasi-two phase system having sharply defined phase boundaries exhibiting micro-fluctuations of electron density within them, taking this fact into consideration we replaced the first term of equation (5) and arrived to the following model:

$$I(q) = \frac{A}{q^n} e^{Bq^2} + \frac{C}{[1+(Lq)^m]} \quad (6)$$

, where A is the Porod's constant, e^{Bq^2} represents the positive deviation to the Porod's law [53], *m* and *n* are the low-*q* and high-*q* scattering exponents, C and L are the multiplicative factor and the correlation length of the Lorentzian term. [52] The attained modified model converges to the experimental data with a $R^2 \approx 0.99999$; parameters *n*, *m* and *L* were obtained by a nonlinear least-squares fit and summarized in **table SI3**.

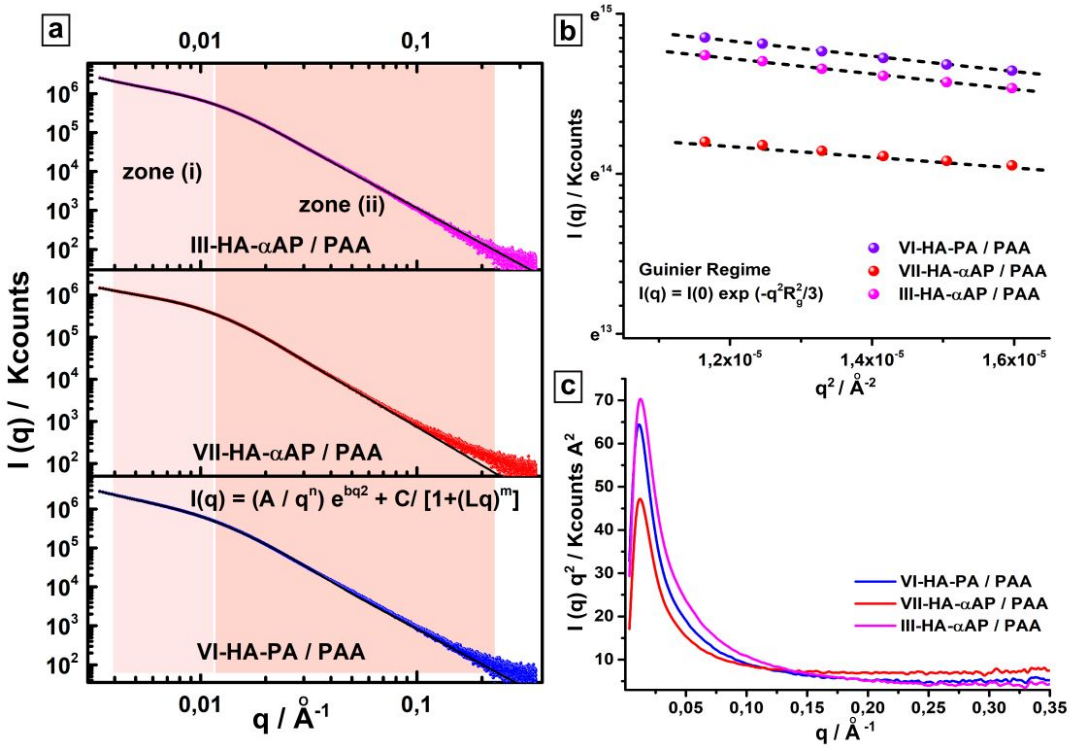

Figure 6. (a) Small angle X-ray scattering (SAXS) profiles of PAA / substituted-HA; color dots are experimental data and black line corresponds to equation (6) model representation. **(b)** Guinier Plot and **(c)** Kratky Plot. RT, pH = 4.1. [OC/HA/W] = [1.5/5/1].

The interpretation of the scattering effect from complex and disordered materials notably simplifies when fractal geometry can be applied in the description of their assembly. The slope of linear parts of *log (I(q)) vs. log (q)* plots can be associated to the mass (D_m), pore

(D_p) and surface (D_s) fractal dimensions. A slope value between -1 and -3 is obtained for volume (mass or pore) fractals while a value of -3 for surface fractals.[53] A slope of about -3 can be associated to collapsed polymer coils and globular domains exhibiting rough surfaces. [30] Scattering exponents obtained by equation (5) in the low- and high-*q* regimes can be interpreted to be representative of the polymer densities observed at these two distinct length scales, [52] and well correlate with mass fractal power-law decay analysis, equation (3). Extra information can be attained by the analysis of Kratky plots, usually used for the qualitatively assess of the flexibility and/or degree of unfolding in samples, [30] **figure 6c**. Figure displays a clear deviation from the horizontal asymptotic behavior and indicates the presence of non-Gaussian characteristic for the scattering chains. [30] Clear peaks at q = 0.0125 Å^{-1} for α-aminophosphonate substituted HA / PAA hydrogels and at q = 0.0106 Å^{-1} for phosphoroamidates substituted HA / PAA hydrogels can be assigned to the presence of folded globular domains in the gel matrix. The amount of the globular domain decreased in the presence of (VII) HA-α-aminophosphonate nanoparticles and reach a maximum for (III)-HA-αAP/PAA hydrogels. Another parameter that supports the trend of increasing local network density is the correlation length, *L*, associated with inter-chain distances in the proximity of individual crosslinking points. We did not find any statistically significant differences among *L* values or in the Kratky plots related to the N-C-P or C-N-P fragment substitution.

Finally we defined an ultra-low q region of 0.003 - 0.004 Å^{-1} to determine the apparent radius of gyration, denoted as R_g^*, by using the least-squares method for the Guinier plot (*ln (I(q))* vs. q^2), **figure 6b**. We did not find statistically significant differences among R_g^* values related to the N-C-P or C-N-P fragment substitution, **figure SI14**, however

differences were observed in the double logarithmic plot slope alongside the Guinier regime. An initial slope of -1 was detected for VII-HA-αAP / PAA-HG, while a slope of ≈ -2 was obtained for VI-HA-PA / PAA-HG and III-HA-αAP / PAA-HG indicating cylindrical and discotic shapes respectively [30] and confirmed that the greatest differences in the organization of polymer chains as a result of the substitution of nanoparticles occurred at global network morphology at scales length > 10 nm and not at local nanostructure. Polarized light microscopy (PLM) was employed to clarify the polymer network structure in the presence of HA and their substituted counterparts. Concentration was progressively increased from homogeneous dilute PAA / HA or functionalized-HA nanoparticles / water (1.5 / 5 / 1 weight ratio) systems by slow evaporation of the solvent (PBS, pH = 7.4) to attain a $\%Wt._{L}$ = 90% (7.5 / 25 / 1 weight ratio) and monitored between crossed polarizers. After completely evaporation, the accurately volume of acetate buffer (pH = 4.1) was injected and the temporal relationship between pH and the evolution of the sample morphology was inspected, **figure SI15**. Under physiological pH conditions and 10 $\%Wt._{H2O}$, PAA chains are randomly suspended and form an isotropic phase between crossed polaroid, **figures 7a** and **7b**, while at pH = 4.1, PAA-HG displays birefringence, **figures 7c** and **7d**. This fact goes along with the coil ⇆ globule polymer transition that occurs at pH = 5, [50] hence the compact structure of the PAA would be related to the formation of a kind of mesoscopic order. In the systems where HA and functionalized-HA nanoparticles are present, birefringence was observed even at pH = 7.4, **figures 7e**, **7f**, **7i**, **7j**, **7m**, **7n**, **7q** and **7r**. The organization of polymer chains at pH = 4.1 and under the influence of nanoparticles exhibits the typical patterns formed by the instabilities of the liquid-crystal / isotropic interface, [54] **figures 7g, 7h, 7k, 7l, 7o, 7p, 7s** and **7t**.

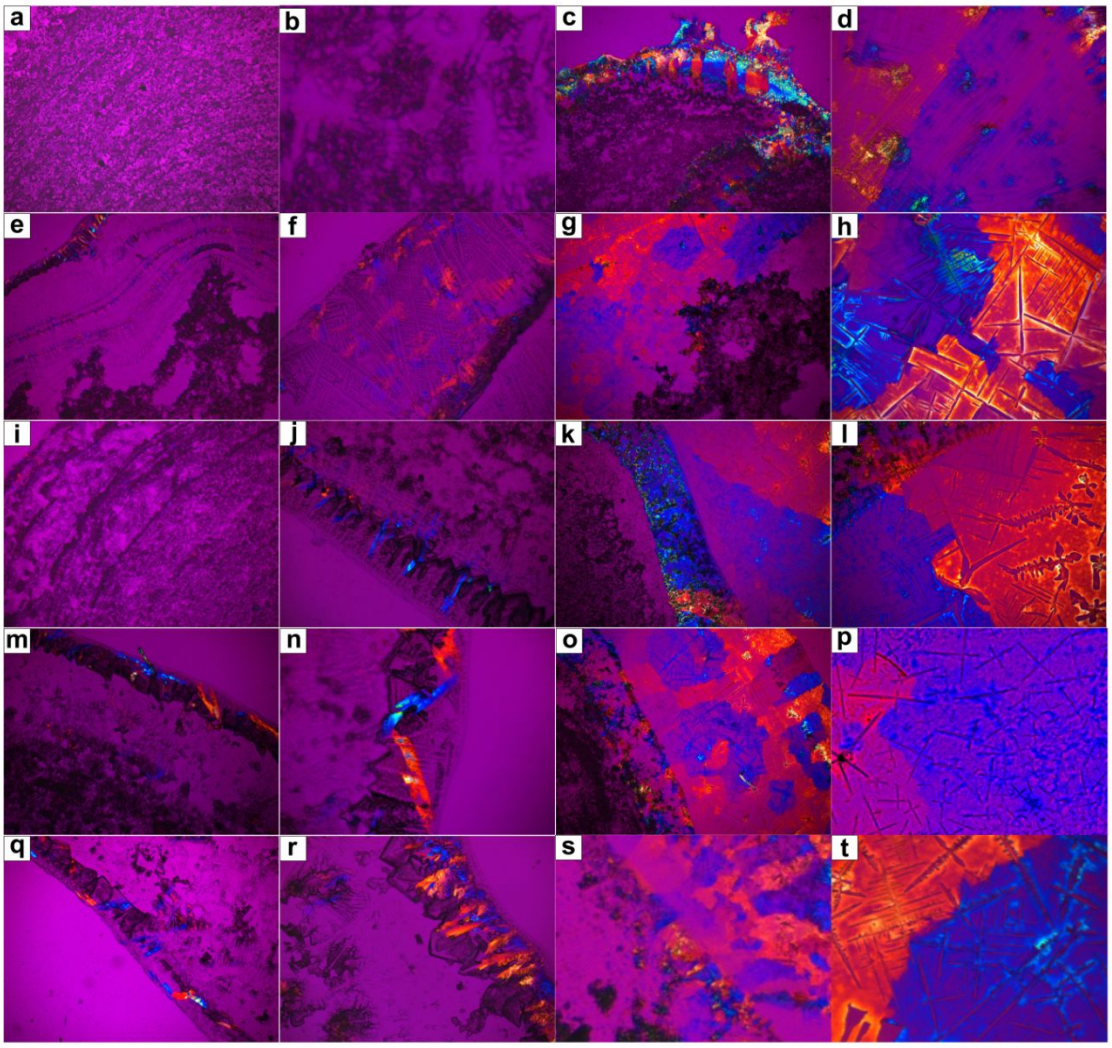

Figure 7. Polarized light microphotographs at RT of (**a, b**) PAA-HG at pH = 7.4; (**c, d**) PAA-HG at pH = 4.1; (**e, f**) HA / PAA-HG at pH = 7.4; (**g, h**) HA / PAA-HG at pH = 4.1; (**i, j**) VI-HA-PA / PAA-HG at pH = 7.4; (**k, l**) VI-HA-PA / PAA-HG at pH = 4.1; (**m, n**) VII-HA-αAP / PAA-HG at pH = 7.4; (**o, p**) VII-HA-αAP / PAA-HG at pH = 4.1; (**q, r**) III-HA-αAP / PAA-HG at pH = 7.4; (**s, t**) III-HA-αAP / PAA-HG at pH = 4.1. Microphotographs were taken under crossed Polaroid and 1 λ retardation plate, after 90% of water evaporation when the final concentration of PAA / water and PAA/ HA, functionalized HA nanoparticles / water was of 7.5 / 1 and 7.5 / 25 / 1 weight ratio respectively. Magnification: 4 × (a, c, e, g, i, k, m, o, q, s) and 20 × (b, d, f, h, j, l, n, p, r, t). For a best interpretation, please refer to on-line version.

PAA-HG at pH = 4.1, **figure 7d**, and HA/PAA-HG or functionalized-HA/PAA-HG at pH = 7.4, **figures 7f, 7j, 7n** and **7r,** displays a dense branching front (BF) pattern described by a nearly straight front bordering a variegated structure. [54] The front is generated by lateral

branches that fill the space creating acute angles forward with the main branch, leaving a pattern of lines (domain limits) that are almost normal to the front. Moreover, under acidic conditions HA/PAA-HG and functionalized-HA/PAA-HG exhibits dense branching (DB) and dendritic (D) patterns, **figures 7h, 7l, 7p** and **7t**. [54] Dense branching morphology is characterized by nearly space filling patterns produced by unstable tips which bifurcate during the growth; the pattern birefringence increases as the texture ripens. [54] Dendrites-like growth is a diffusion-controlled process in the presence of anisotropy, [55] i.e. an appropriate degree of anisotropy must be present for steady-state dendrites to exist [56, 57] and it is a key parameter affecting the evolution of the crystalline morphology. [58] Dense branching (DB) and dendritic (D) patterns are observed only in those samples that enclose nanoparticles, which allow us to conclude that they are the physical mesogenic agents; an example was shown in **figure 8**. Shapes started to grow from a seed at the central region forming a four-pointed cross, **figures 8a (i)** and **8c (i)**. From the original cross, there is a new bifurcation of their branches that occurs in straight or degenerate subdivisions; the secondary arms growth rigorously perpendicular to the primary arm. Straight branches grow and divide again into parallel lines forming plates, **figures 8a (iii)**, **8b (iii)** and **8c (iii)**; while degenerate subdivision originates neuronal-type patterns, **figure 8c (ii)**.

Columnar phases forming from the isotropic melt often exhibit dendritic-like growth aggregates, [59, 60] sometimes directly reflecting the generally six fold symmetry of their constituent's molecules. Here we are in the presence of lyotropic and not of thermotropic liquid crystals, and dendritic structures were observed in the highest concentration solutions.

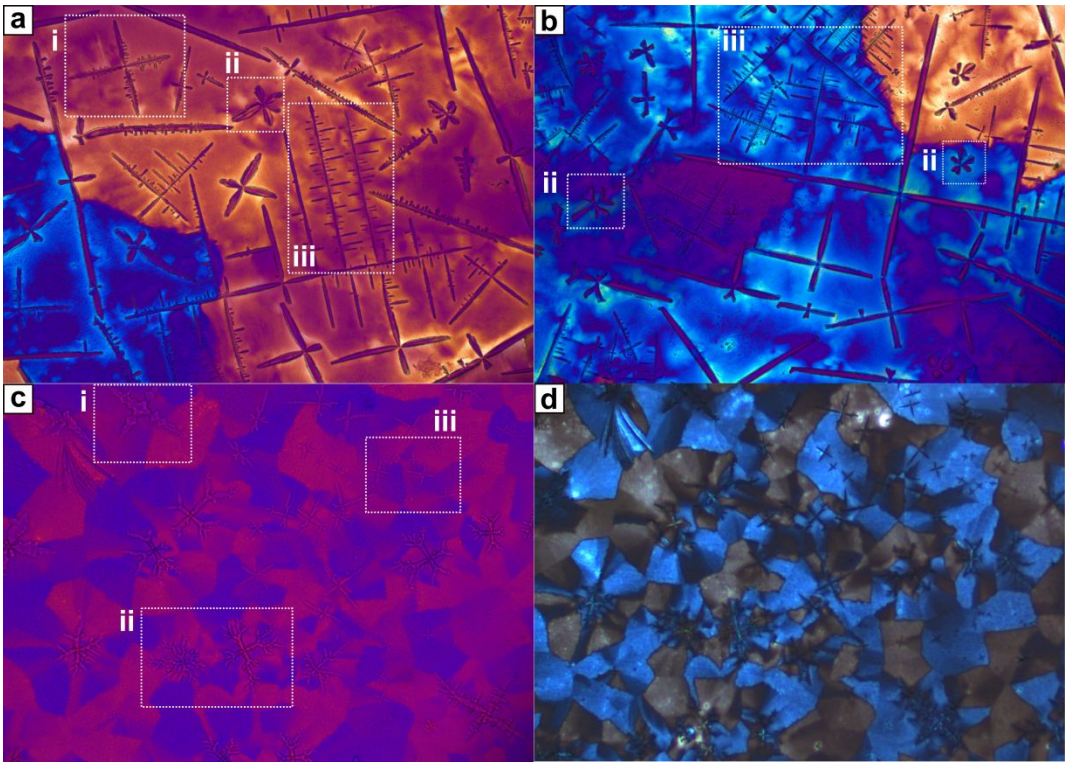

Figure 8. Dendritic patters in VI-HA-PA / PAA-HG at pH = 4.1 and RT. (**i**) four-pointed cross grow from a central seed forming dendritic branches; (**ii**) degenerate subdivision, neuronal type structures; (**iii**) straight-lined subdivisions, paralleled cross-lined patterns. Microphotographs were taken after 90% of water evaporation when the final concentration of PAA/ VI-HA-PA / water was of 7.5 / 2.5/ 1 weight ratio. Operational conditions: (**a, b** and **c**) crossed Polaroid and 1λ retardation plate; (**d**) crossed Polaroid, without retardation plate. Magnification: 20×. For a best interpretation, please refer to on-line version.

Between crossed polarizers lyotropic hexagonal phase textures are similar to that of hexagonal columnar phase in discotic liquid crystals. [61] **Figure 8d**, shows the typical flower-like domains of mono-tropic hexagonal columnar mesophase, [60] although not perfectly ordered. Note that in the samples observed without the retardation plate and crossed polarizers, each dendrite is in the center of this characteristic texture, **figure 8d**.

This type of structure was observed both for VI-HA-PA / PAA-HG and III-HA-αAP / PAA-HG samples at pH = 4.1 where it was confirmed by SAXS a flat disks globular organization of the polymer chains at scale length > 10 nm. Literature data reported the

existence of a particular crystalline liquid configuration, denoted as *"discotic disordered hexagonal"* related to the uncommon molecular structure of the discogen.[62] According to the results obtained, we believe that we are in the presence of this type of structures.

4. Conclusions

Along the present study we have established synthetic routes for the anchorage of N-C-P and C-N-P molecular fragments on the nano-HA surface and demonstrated that the grafted nano-HA acted as a mesogenic agent influencing the structure and organization of acidic macromolecules as happening in nature. Different experimental conditions based on the surface silanization mediated by APTES, APTES-phosphoroamidates and APTES-α-aminophosphonate were tested and compared. It was confirmed that obtained products follows a Si-O bond formation between nano-HA superficial water clusters followed by the polycondensation of hydrolyzed attached APTES derivative. Substituted-HA nanoparticles showed a greater cohesion capacity around acidic chains macromolecules than bare nano-HA. We did not notice statistically significant differences related to the N-C-P or C-N-P molecular fragment; however, we observed dissimilarities associated to the degree of substitution. VI-HA-PA and III-HA-αAP adducts, exhibiting a degree of substitution superior than VII-HA-αAP, induced the formation of lyotropic bio-inspired self-organized phases when they were added in a concentration analogous to those found in bone tissue. Textures observed under a polarized light microscope resemble distorted columnar mesophase that well correlated with the presence of a discotic globular organization of polymer chains at scale length > 10 nm.

As a general point of view, the obtained results increase the offer of inorganic mesogenic agents and expand the universe of applications of lyotropic liquid crystals. In particular, the successful self-organization of acidic macromolecules under the stimuli of hydroxyapatite nanoparticles grafted with fragments of phosphorus derivatives is a crucial step in conquering the regeneration of calcified tissues.

Acknowledgements: The authors acknowledge the financial support of Universidad Nacional del Sur (UNS, PGI 24/Q092), Concejo Nacional de Investigaciones Científicas y Técnicas (CONICET, PIP – 11220130100100CO), Agencia Nacional de Promoción Científica y Tecnológica (ANPCyT, PICT 201-0126), Comisión de Investigaciones Científicas (CIC), Argentina and Xunta de Galicia (AEMAT, ED431E2018/08 and ED431B2017/21). SN has a Training Scholarship (BENTR 2019) awarded by the CIC. LAB, YM and PVM are researchers of CONICET.

Supporting Information: It contains additional information related of the HA-phosphorus derivative synthesis, thermodynamic behaviour, SAXS data analysis and crystalline liquid morphology of HA/PAA- HG.

References

(1) Saw, T. B.; Xi, W.; Ladoux, B.; Lim, C. T., Biological Tissues as Active Nematic Liquid Crystals. *Adv. Mater.* **2018,** 30, (47), 1802579.

(2) Sung, B.; Kim, M.-H., Liquid-crystalline nanoarchitectures for tissue engineering. *Beilstein J. Nanotechnol.* **2018,** 9, (1), 205-215.

(3) Mitov, M., Cholesteric liquid crystals in living matter. *Soft Matter* **2017,** 13, (23), 4176-4209.

(4) Landis, W. J., The strength of a calcified tissue depends in part on the molecular structure and organization of its constituent mineral crystals in their organic matrix. *Bone* **1995,** 16, (5), 533-544.

(5) Tan, J.; Jin, X.; Chen, M., Bio-inspired synthesis of aqueous nanoapatite liquid crystals. *Sci. Rep.* **2019,** 9, (1), 466.

(6) Yang, C.; Zhao, C.; Wang, X.; Shi, M.; Zhu, Y.; Jing, L.; Wu, C.; Chang, J., Stimulation of osteogenesis and angiogenesis by micro/nano hierarchical hydroxyapatite via macrophage immunomodulation. *Nanoscale* **2019,** 11, (38), 17699-17708.

(7) de Souza, J. F.; Pontes, K. d. S.; Alves, T. F. R.; Amaral, V. A.; Rebelo, M. d. A.; Hausen, M. A.; Chaud, M. V., Spotlight on Biomimetic Systems Based on Lyotropic Liquid Crystal. *Molecules* **2017,** 22, (3), 419.

(8) Hoshino, T.; Nakayama, M.; Fujinami, S.; Nakatani, T.; Kohmura, Y.; Kato, T., Static structure and dynamical behavior of colloidal liquid crystals consisting of hydroxyapatite-based nanorod hybrids. *Soft Matter* **2019,** 15, (16), 3315-3322.

(9) Nakayama, M.; Kajiyama, S.; Kumamoto, A.; Nishimura, T.; Ikuhara, Y.; Yamato, M.; Kato, T., Stimuli-responsive hydroxyapatite liquid crystal with macroscopically controllable ordering and magneto-optical functions. *Nature Commun.* **2018,** 9, (1), 568.

(10) D'Elía, N. L.; Mathieu, C.; Hoemann, C. D.; Laiuppa, J. A.; Santillán, G. E.; Messina, P. V., Bone-repair properties of biodegradable hydroxyapatite nano-rod superstructures. *Nanoscale* **2015,** 7, (44), 18751-18762.

(11) Placente, D.; Benedini, L. A.; Baldini, M.; Laiuppa, J. A.; Santillán, G. E.; Messina, P. V., Multi-drug delivery system based on lipid membrane mimetic coated nano-hydroxyapatite formulations. *Int. J. Pharm.* **2018,** 548, (1), 559-570.

(12) Placente, D.; Ruso, J. M.; Baldini, M.; Laiuppa, J. A.; Sieben, J. M.; Santillán, G. E.; Messina, P. V., Self-fluorescent antibiotic MoO x–hydroxyapatite: a nano-theranostic platform for bone infection therapies. *Nanoscale* **2019,** 11, (37), 17277-17292.

(13) Sartuqui, J.; Gravina, A. N.; Rial, R.; Benedini, L. A.; Yahia, L. H.; Ruso, J. M.; Messina, P. V., Biomimetic fiber mesh scaffolds based on gelatin and hydroxyapatite nano-rods: Designing intrinsic skills to attain bone reparation abilities. *Colloids Surf., B* **2016,** 145, 382-391.

(14) Benedini, L.; Placente, D.; Pieroni, O.; Messina, P., Assessment of synergistic interactions on self-assembled sodium alginate/nano-hydroxyapatite composites: to the conception of new bone tissue dressings. *Colloid Polym. Sci.* **2017,** 295, (11), 2109-2121.

(15) D'Elía, N. L.; Rial Silva, R.; Sartuqui, J.; Ercoli, D.; Ruso, J.; Messina, P.; Mestres, G., Development and characterisation of bilayered periosteum-inspired composite membranes based on sodium alginate-hydroxyapatite nanoparticles. *J. Colloid Interface Sci.* **2020,** 572, 408-420.

(16) D'Elia, N. L.; Gravina, N.; Ruso, J. M.; Marco-Brown, J. L.; Sieben, J. M.; Messina, P. V., Albumin-mediated deposition of bone-like apatite onto nano-sized surfaces: Effect of surface reactivity and interfacial hydration. *J. Colloid Interface Sci.* **2017,** 494, 345-354.

(17) Rial, R. n.; Tichnell, B.; Latimer, B.; Liu, Z.; Messina, P. V.; Ruso, J. M., Structural and kinetic visualization of the protein corona on bioceramic nanoparticles. *Langmuir* **2018,** 34, (7), 2471-2480.
(18) Contreras-García, A.; D'Elía, N. L.; Desgagné, M.; Lafantaisie-Favreau, C.-H.; Rivard, G.-E.; Ruiz, J.-C.; Wertheimer, M. R.; Messina, P.; Hoemann, C. D., Synthetic anionic surfaces can replace microparticles in stimulating burst coagulation of blood plasma. *Colloids Surf., B* **2019,** 175, 596-605.
(19) Sartuqui, J.; D'Elía, N. L.; Ercoli, D.; de Alcazar, D. S.; Cortajarena, A. L.; Messina, P. V., Mechanical performance of gelatin fiber mesh scaffolds reinforced with nano-hydroxyapatite under bone damage mechanisms. *Mater. Today Commun.* **2019,** 19, 140-147.
(20) Thakur, V. K.; Kessler, M. R., *Liquid crystalline polymers*. ed.; Springer: 2016; Vol. Structure and Chemistry, p 626.
(21) Mucha, A.; Kafarski, P.; Berlicki, Ł., Remarkable Potential of the α-Aminophosphonate/Phosphinate Structural Motif in Medicinal Chemistry. *J. Med. Chem.* **2011,** 54, (17), 5955-5980.
(22) Cremers, S.; Drake, M. T.; Ebetino, F. H.; Bilezikian, J. P.; Russell, R. G. G., Pharmacology of bisphosphonates. *Br. J. Clin. Pharmacol.* **2019,** 85, (6), 1052-1062.
(23) Wang, S.; Wen, S.; Shen, M.; Guo, R.; Cao, X.; Wang, J.; Shi, X., Aminopropyltriethoxysilane-mediated surface functionalization of hydroxyapatite nanoparticles: synthesis, characterization, and in vitro toxicity assay. *Int. J. Nanomed.* **2011,** 6, 3449-3459.
(24) Russo, L.; Taraballi, F.; Lupo, C.; Poveda, A.; Jiménez-Barbero, J.; Sandri, M.; Tampieri, A.; Nicotra, F.; Cipolla, L., Carbonate hydroxyapatite functionalization: a comparative study towards (bio) molecules fixation. *Interface Focus* **2014,** 4, (1), 20130040.
(25) Zhao, Y.; Chen, X.; Chen, T.; Zhou, Y.; Yin, S.-F.; Han, L.-B., Catalyst-Free and Selective C–N Bond Functionalization: Stereospecific Three-Component Coupling of Amines, Dichloromethane, and> P (O) H Species Affording α-Aminophosphorus Compounds. *J. Org. Chem.* **2015,** 80, (1), 62-69.
(26) Dudarko, O.; Zub, Y. L.; Semenii, V. Y.; Dabrowski, A., The preparation of polysiloxane xerogels containing amide derivatives of phosphonic and thiophosphonic acids in the surface layer. *Colloid J.* **2007,** 69, (1), 66-74.
(27) Kaletunç, G., *Calorimetry in food processing: analysis and design of food systems*. ed.; John Wiley & Sons: 2009; Vol. 39.
(28) Peixoto, P. D. S.; Deniset-Besseau, A.; Schanne-Klein, M.-C.; Mosser, G., Quantitative assessment of collagen I liquid crystal organizations: role of ionic force and acidic solvent, and evidence of new phases. *Soft Matter* **2011,** 7, (23), 11203-11210.
(29) Feng, X., Chemical and Biochemical Basis of Cell-Bone Matrix Interaction in Health and Disease. *Curr. Chem. Biol.* **2009,** 3, (2), 189-196.
(30) Ochbaum, G.; Bitton, R., Using small-angle X-ray scattering (SAXS) to study the structure of self-assembling biomaterials. In *Self-assembling Biomaterials*, Elsevier: 2018; pp 291-304.
(31) Kohls, D. J.; Beaucage, G., Rational design of reinforced rubber. *Curr. Opin. Solid State Mater. Sci.* **2002,** 6, (3), 183-194.
(32) Stoline, M. R., The status of multiple comparisons: simultaneous estimation of all pairwise comparisons in one-way ANOVA designs. *Am Stat.* **1981,** 35, (3), 134-141.
(33) Siniscalco, D.; Dutreilh-Colas, M.; Hjezi, Z.; Cornette, J.; El Felss, N.; Champion, E.; Damia, C., Functionalization of hydroxyapatite ceramics: Raman mapping investigation of silanization. *Ceramics* **2019,** 2, (2), 372-384.

(34) Sartuqui, J.; Gardin, C.; Ferroni, L.; Zavan, B.; Messina, P., Nanostructured hydroxyapatite networks: Synergy of physical and chemical cues to induce an osteogenic fate in an additive-free medium. *Mater. Today Commun.* **2018,** 16, 152-163.

(35) Grunenwald, A.; Keyser, C.; Sautereau, A.-M.; Crubézy, E.; Ludes, B.; Drouet, C., Revisiting carbonate quantification in apatite (bio) minerals: a validated FTIR methodology. *J. Archaeol. Sci.* **2014,** 49, 134-141.

(36) Mathew, R.; Gunawidjaja, P. N.; Izquierdo-Barba, I.; Jansson, K.; García, A.; Arcos, D.; Vallet-Regí, M.; Edén, M., Solid-state 31P and 1H NMR investigations of amorphous and crystalline calcium phosphates grown biomimetically from a mesoporous bioactive glass. *J. Phys. Chem. C* **2011,** 115, (42), 20572-20582.

(37) Jäger, C.; Welzel, T.; Meyer-Zaika, W.; Epple, M., A solid-state NMR investigation of the structure of nanocrystalline hydroxyapatite. *Magn. Reson. Chem.* **2006,** 44, (6), 573-580.

(38) Von Euw, S.; Wang, Y.; Laurent, G.; Drouet, C.; Babonneau, F.; Nassif, N.; Azais, T., Bone mineral: new insights into its chemical composition. *Sci. Rep.* **2019,** 9.

(39) Wilson, E. E.; Awonusi, A.; Morris, M. D.; Kohn, D. H.; Tecklenburg, M. M.; Beck, L. W., Three structural roles for water in bone observed by solid-state NMR. *Biophys. J.* **2006,** 90, (10), 3722-3731.

(40) Okada, M.; Matsumoto, T., Synthesis and modification of apatite nanoparticles for use in dental and medical applications. *Jpn. Dent. Sci. Rev.* **2015,** 51, (4), 85-95.

(41) Lee, D.; Monin, G.; Duong, N. T.; Lopez, I. Z.; Bardet, M.; Mareau, V.; Gonon, L.; De Paëpe, G. l., Untangling the condensation network of organosiloxanes on nanoparticles using 2D 29Si–29Si solid-state NMR enhanced by dynamic nuclear polarization. *J. Am. Chem. Soc.* **2014,** 136, (39), 13781-13788.

(42) Alvares, K., The role of acidic phosphoproteins in biomineralization. *Connect. Tissue Res.* **2014,** 55, (1), 34-40.

(43) Kalka, M.; Zoglowek, A.; Ożyhar, A.; Dobryszycki, P., Proteins in Calcium Phosphate Biomineralization. In *Calcium Phosphates-From Fundamentals to Applications*, IntechOpen: 2019.

(44) Fujisawa, R.; Tamura, M., Acidic bone matrix proteins and their roles in calcification. *Front. Biosci., Scholar Ed.* **2012,** 17, 1891-903.

(45) Maurer, J.; Eustace, D.; Ratcliffe, C., Thermal characterization of poly (acrylic acid). *Macromolecules* **1987,** 20, (1), 196-202.

(46) Gavrilova, N. D.; Malyshkina, I. A.; Makhaeva, E. E.; Novik, V. K.; Vorobiev, A. V., Dielectric relaxation anomalies in polyacrylic acid and their relationship with “critical” points of water. *Ferroelectrics* **2016,** 504, (1), 3-14.

(47) Singh, B.; Dhiman, A., Functionalization of carbopol with NVP for designing antibiotic drug loaded hydrogel dressings for better wound management. *J. Pharm. Biopharm. Res.* **2019,** 1, (1), 1-14.

(48) Gun’ko, V.; Savina, I.; Mikhalovsky, S., Properties of water bound in hydrogels. *Gels* **2017,** 3, (4), 37.

(49) Bag, M.; Valenzuela, L., Impact of the hydration states of polymers on their hemocompatibility for medical applications: A review. *Int. J. Mol. Sci.* **2017,** 18, (8), 1422.

(50) Swift, T.; Swanson, L.; Geoghegan, M.; Rimmer, S., The pH-responsive behaviour of poly (acrylic acid) in aqueous solution is dependent on molar mass. *Soft Matter* **2016,** 12, (9), 2542-2549.

(51) Panyukov, S.; Rabin, Y., Statistical physics of polymer gels. *Phys. Rep.* **1996,** 269, (1), 1-131.

(52) Hule, R. A.; Nagarkar, R. P.; Altunbas, A.; Ramay, H. R.; Branco, M. C.; Schneider, J. P.; Pochan, D. J., Correlations between structure, material properties and bioproperties in self-assembled β-hairpin peptide hydrogels. *Faraday Discuss.* **2008,** 139, 251-264.

(53) Li, Z.-H., A program for SAXS data processing and analysis. *Chin. Phys. C* **2013,** 37, (10), 108002.
(54) Arora, S.; Buka, A.; Palffy-Muhoray, P.; Racz, Z.; Vora, R., Pattern formation during mesophase growth in liquid crystals. *Europhys. Lett.* **1988,** 7, (1), 43.
(55) Gleeson, J., Dendritic growth of electro-hydrodynamic convection in a nematic liquid crystal. *Nature* **1997,** 385, (6616), 511-513.
(56) Oswald, P.; Bechhoefer, J.; Melo, F., Pattern Formation During the Growth of Liquid Crystal Phases. *MRS Bull.* **1991,** 16, (1), 38-45.
(57) Von Kurnatowski, M.; Kassner, K., Selection theory of dendritic growth with anisotropic diffusion. *Adv. Condens. Matter Phys.* **2015,** 2015, (ID 529036), 1-6.
(58) Hou, H.; Zhao, Y.-h.; Niu, X.-f., 3D anisotropy simulation of dendrites growth with phase field method. *Trans. Nonferrous Met. Soc. China* **2008,** 18, (s1), s223-s228.
(59) Oswald, P., Dendritic growth of a discotic liquid crystal. *J. Phys. (France)* **1988,** 49, (7), 1083-1089.
(60) Ferreira, M.; Westphal, E.; Ballottin, M.; Bechtold, I.; Bortoluzzi, A.; Mezalira, D.; Gallardo, H., Columnar bent-core liquid crystals with two oxadiazole units and two or four alkyl chains and their phase-dependent fluorescence. *New J. Chem.* **2017,** 41, (20), 11766-11777.
(61) Collings, P.; Hird, M., *Introduction to Liquid Crystals: Chemistry and Physics*. ed.; CRC PRESS: 2019.
(62) Yoneya, M.; Makabe, T.; Miyamoto, A.; Shimizu, Y.; Miyake, Y.; Yoshida, H.; Fujii, A.; Ozaki, M., Tilt orientationally disordered hexagonal columnar phase of phthalocyanine discotic liquid crystals. *Phys. Rev. E* **2014,** 89, (6), 062505.

Table of Contents (TOC)/Abstract Graphic